References and Notes

1. J. Faist *et al*., *Science* **264**, 553 (1994).
2. F. Capasso, C. Gmachl, D. L. Sivco, A. Y. Cho, *Phys. World* **12**, 27 (1999).
3. F. Capasso, *Science* **235**, 172 (1987).
4. A. Y. Cho Ed., *Molecular Beam Epitaxy* (AIP Press, Woodbury, NY, 1994).
5. C. Gmachl *et al*., *IEEE J. Select. Topics Quantum Electron.*, **5**, 808 (1999).
6. Certain bipolar semiconductor lasers, when biased in reverse polarity, can function as photodetectors, as has recently been demonstrated (*19*).
7. J. Faist *et al*., *Nature* **387**, 777 (1997).
8. This requirement makes the task of designing the bidirectional laser more difficult, as in general the applied electric field across any QC laser scales linearly with the energy of the optical transition.
9. J. Faist *et al*., *Appl. Phys. Lett.* **68**, 3680 (1996).
10. J. Faist *et al*., *IEEE J. Quantum Electron.* **34**, 336 (1998).
11. A. Tredicucci *et al*., *Appl. Phys. Lett.* **72**, 2388 (1998).
12. C. Sirtori *et al*., *ibid.* **66**, 3242 (1995).
13. The discrepancy in λ_+ (λ_-) corresponds to an applied bias 0.09 V (0.64 V) higher than the design value, which results in a relative difference in the threshold voltage of only 0.55 V. This is in reasonable agreement with the experiment and its uncertainties.
14. A. Tredicucci *et al*., *Nature* **396**, 350 (1998), and references (*3*–*7*) therein.
15. M. W. Sigrist, *Air Monitoring by Spectroscopic Techniques* (Wiley, New York, 1994), chap. 3 and 5.
16. For applications of QC lasers in general, a high operating temperature is highly desirable. Although operation up to room temperature is readily achieved in a pulsed, low–duty-cycle mode (*5*), continuous wave operation is at present limited to temperatures below 175 K (*20*). Promising proposals for improvements exist, for example, through suppression of the nonradiative recombination pathways (*21, 22*).
17. B. H. Yang *et al*., *Appl. Phys. Lett.* **72**, 2220 (1998).
18. L. Olafsen *et al*., *ibid*., p. 2370.
19. D. A. Louderback, O. Sjölund, E. R. Hegblom, J. Ko, L. A. Coldren, *IEEE Photonics Technol. Lett.* **11**, 304 (1999).
20. C. Gmachl *et al*., *ibid*., in press.
21. C. F. Hsu, J. S. O, P. S. Zory, D. Botez, *Proc. SPIE* **3001**, 271 (1997).
22. K. W. Berryman, S. A. Lyon, M. Segev, J. R. Engholm, in *IEEE/OSA CLEO'99 Conference* (Optical Society of America, Washington, DC, 1999), p. 52.

23. We are grateful to S. N. G. Chu for his help with material characterization, in particular transmission electron microscopy, and to H. Kogelnik for stimulating discussions. This work has been supported in part by the Defense Advanced Research Projects Agency/U.S. Army Research Office under contract DAAG55-98-C-0050.

18 June 1999; accepted 15 September 1999

Asymmetric Electrical Structure in the Mantle Beneath the East Pacific Rise at 17°S

R. L. Evans,[1]* P. Tarits,[2] A. D. Chave,[1] A. White,[3] G. Heinson,[3] J. H. Filloux,[4] H. Toh,[5] N. Seama,[6] H. Utada,[7] J. R. Booker,[8] M. J. Unsworth[8]

The magnetotelluric component of the Mantle Electromagnetic and Tomography (MELT) Experiment measured the electrical resistivity structure of the mantle beneath the fast-spreading southern East Pacific Rise (EPR). The data reveal an asymmetric resistivity structure, with lower resistivity to the west of the ridge. The uppermost 100 kilometers of mantle immediately to the east of the ridge is consistent with a dry olivine resistivity structure indicating a mantle depleted of melt and volatiles. Mantle resistivities to the west of the ridge are consistent with a low-melt fraction (about 1 to 2 percent interconnected melt) distributed over a broad region and extending to depths of about 150 kilometers. The asymmetry in resistivity structure may be the result of asymmetric spreading rates and a westward migration of the ridge axis and suggests distinct styles of melt formation and delivery in the mantle beneath the two plates.

The generation of new oceanic crust at midocean ridges involves the production and transport of melt from a source region deep within the mantle and its subsequent emplacement over a narrow zone centered beneath the ridge axis. The lateral and depth extents of the melt source region and the mode of melt delivery are not well determined. Geochemical data indicate that most melting occurs above 60 km (*1*), although there have been suggestions of a contribution from within the garnet stability field at greater depth (*2*). In addition, incompatible trace elements found in midocean ridge basalt (MORB) suggest that deeper melting at around 200 km may occur in the presence of water (*3*). There are fewer data that constrain the mode of melt transport, and hence recourse must be made to models. Numerical models for melt generation and mantle flow have demonstrated a variety of flow patterns that ensue from the competing effects of passive plate-driven upwelling, buoyancy forces from melt and the depleted residual mantle (*4*), and rheological variations that are controlled by temperature (*5*), melt fraction (*6*), and the presence of volatiles (*7*). In a passive flow regime with efficient melt transport, low-melt fractions (above 0.3%) are predicted within a broad melting region extending 100 km or more off-axis. As the buoyancy effects of melt become important, especially at lower spreading rates, more tightly focused melt delivery is achieved beneath the ridge with a depleted residual mantle produced just off-axis (*5*). Additionally, models that incorporate deeper incipient melting have been proposed with upwelling beginning at around 200-km depth and delivery of a small melt fraction to the ridge crest as part of a small-scale convective flow with a 200-km-length scale (*5*).

The MELT geophysical experiment (*8*), carried out at 17°S on the EPR, used seismic and electromagnetic observations to determine the geometry of the region of partial melting and the pattern of upwelling beneath a ridge, elucidate the melt concentration within that region, and determine the distribution and connectedness of melt in the rock matrix. The EPR near 17°S was chosen as the site for the MELT Experiment based on its fast (~150 mm/year) spreading rate and linear ridge morphology which, based on numerical models, was expected to maximize the two-dimensionality of mantle flow. However, the ridge has been shown to exhibit asymmetric spreading, with faster absolute plate motion on the Pacific plate resulting in a slow westward migration of the ridge axis with respect to the hot-spot reference frame. This asymmetry is manifest as lower subsidence of the sea floor with distance from the ridge to the west than to the east, and a greater abundance of seamounts on the Pacific plate than on the Nazca plate (*9*, *10*). The seismic component of MELT was completed in 1996 (*11*–*15*), and a key result from those analyses is that melt generation and transport occur over a broad region of the mantle, with no evidence found for a narrow column of melt beneath the ridge that would indicate highly focused melt delivery. Asymmetry between the eastern and western sides of the ridge is seen (*12*), with a zone of 1 to 2% melt inferred in the top 100 km of mantle extending some 300 to 400 km to the west of the ridge but only 150 km to the east (*11*–*13*). Reduced shear-wave velocities extend to depths in excess of 100 km, with a steep gradient in velocity between 100 and 180 km (*14*).

Here, we present initial results from the

[1]Woods Hole Oceanographic Institution, Woods Hole, MA 02543, USA. [2]UMR CNRS 6538, Universite Bretagne Occidentale, Brest, France. [3]Flinders University, Adelaide, South Australia 5042, Australia. [4]Scripps Institution of Oceanography, La Jolla, CA 92093, USA. [5]Toyama University, Toyama 930-8555, Japan. [6]Chiba University, Chiba, Japan. [7]Earthquake Research Institute, University of Tokyo, Tokyo 113, Japan. [8]Geophysics Program AK-50, University of Washington, Seattle, WA 98195, USA.

*To whom correspondence should be addressed. E-mail: revans@whoi.edu

magnetotelluric (MT) component of the experiment and their implications for melt generation and flow beneath the EPR. The MT technique uses simultaneous time variations of the naturally induced sea-floor electric and magnetic fields to infer the electrical resistivity structure of the mantle. The electrical resistivity of the mantle responds to a variety of factors such as temperature, but is expected to be reduced in the presence of partial melt, provided the melt forms an interconnected network (*16*). There is also evidence that water, in the form of dissolved hydrogen, decreases mantle resistivity (*17*). Water plays a key role in mantle melting processes by lowering the temperature of the solidus and also affects the rheology of the upwelling mantle (*18*).

From June 1996 to June 1997, 47 sea-floor instruments measured the time variations of the electric and magnetic fields at 32 sites along two east-west lines in the MELT area. Instrumental principles are reviewed by Filloux (*19*). Two lines were occupied, the most heavily sampled of which crossed the EPR at 17°S on a magma-rich segment of ridge (Fig. 1) and consisted of 19 sites extending 200 km on either side of the ridge crest at spacings ranging from 3 km at the axis to 75 km at the extremes. The second line crossed the EPR at about 15°45′S to the north of an overlapping spreading center on a magma-starved ridge segment and consisted of 13 sites extending 100 km on either side of the axis. Here we present the results for data collected at 11 sites along the 17°S transect. Data coverage more than 100 km west of the ridge axis is limited by instrument failures. Processing of the electric and magnetic field time series followed standard procedures (*20*).

Over a two-dimensional (2D) resistivity structure it is possible to describe the full MT tensor in terms of two principal modes, corresponding to electric currents that flow either parallel to the ridge (TE mode) or in vertical loops whose plane is oriented perpendicular to strike (TM mode). Because of the physics of each mode, they are sensitive to mantle structure beneath the ridge in different ways (*21*). In general, the TM mode responds mostly to the background mean structure of the mantle and is expected to be less sensitive than the TE mode to the presence of a melt column beneath the ridge. This relation means that jointly interpreting the two modes can provide tighter constraints on the regional resistivity structure than looking at either mode on its own.

As for most MT data, the sea-floor electromagnetic fields were expected to be distorted by surface structures, in this case principally the rugged EPR bathymetry (Fig. 1). This phenomenon can be treated in standard ways (*22*). The influence of topography poses significant problems for modeling as it is difficult to simultaneously incorporate into a single numerical model of resistivity structure the small-scale (relative to the induction scale) bathymetry that produces distortion, as well as the much larger scale and presumably heterogeneous structures of the underlying mantle.

Because no model can account for surface distortion perfectly, two independent approaches were adopted to deal with its effects. The first incorporates a simplified regional scale, 2D representation of bathymetry into all forward calculations of the sea-floor MT response. The observed data were modeled with the rapid relaxation inversion (RRI) algorithm (*23*). The RRI algorithm seeks maximally smooth resistivity models satisfying a data constraint at a specified level of misfit. The initial steps in model space focus on reducing the global misfit, after which the algorithm concentrates on

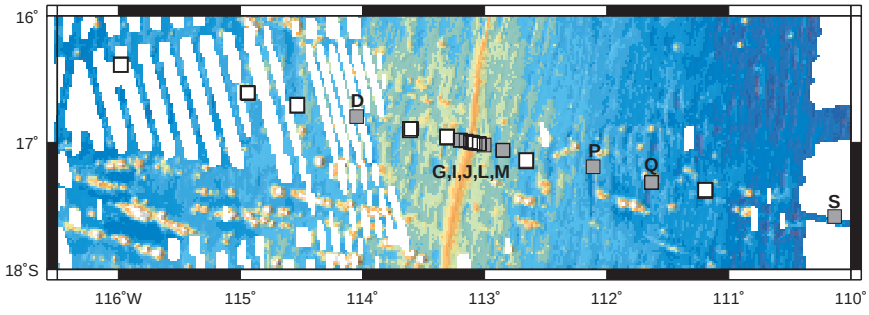

Fig. 1. A map of the EPR near 17°S showing the southern of two lines of sea-floor MT sites occupied during the MELT Experiment. The MT array was aligned perpendicular to the strike of the ridge to maximize the two-dimensionality of the experiment; this is in contrast to the seismic array, which was oriented toward the region of maximum earthquake activity (*11*). The 11 sites for which data have been used in the present analysis are shown by the labeled, filled squares. The station names in the map refer to the locations of the magnetometers used for MT tensor estimation. In some cases, electric field data from adjacent sites were used rather than colocated ones. This was accounted for in all subsequent data modeling.

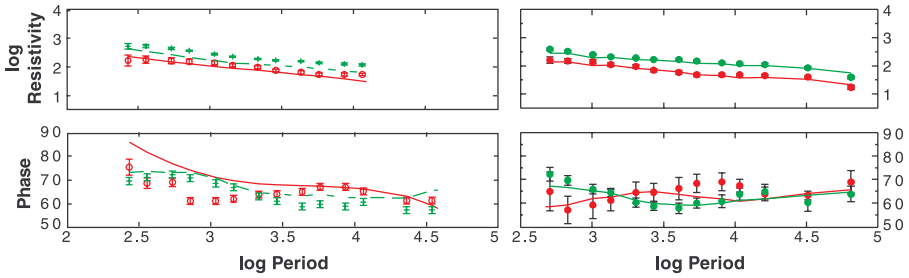

Fig 2. Sample fits to the data for site L, which was 6 km to the east of the ridge axis. The TE mode data are shown in red and the TM data in green. Data with and without topographic stripping are shown along with their respective model responses. Note the substantial change in the TE mode phase in particular when the topographic effect is removed.

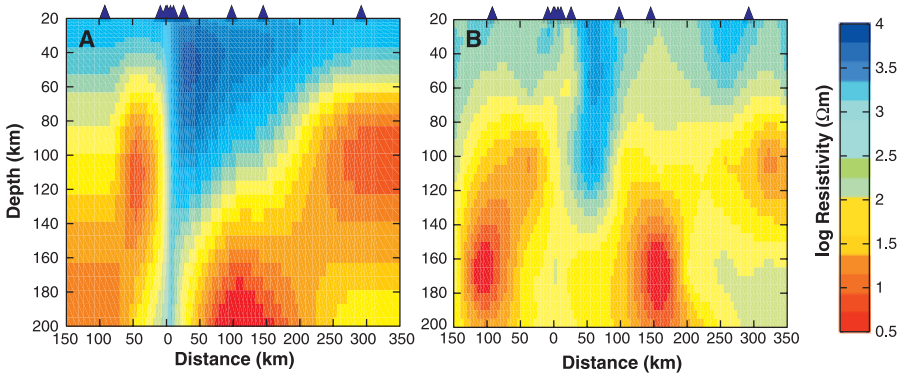

Fig 3. Two inverse models arrived at by independent means. (**A**) was obtained by inverting the raw TE and TM mode data and including 2D sea-floor topography in the forward calculations. (**B**) was obtained through inversion of an MT tensor that has had the predictable effects of the full sea-floor topography removed by using the thin-sheet approximation.

reducing the roughness of the resistivity model. The forward calculation was modified for the MELT data by allowing electric and magnetic fields at different sea-floor locations to be used to calculate the model MT tensor. The simultaneous inversion of both TE and TM modes starts with a uniform sea-floor half-space plus topography and iterates toward a minimum achievable misfit (*24*). The choice of final model was based both on global misfit and the fits at individual stations. Although it is possible to achieve lower misfit by inverting the modes separately, the first-order features that are the most robust also appear in the individual mode inversions. Examples of fits for the TE+TM inversion at station L, just to the east of the ridge crest, are shown in Fig. 2, while the final preferred RRI model is shown in Fig. 3A.

The second approach used a thin-sheet model (*25*) to remove the effects of 3D bathymetry from the MT tensor, yielding values corrected to a flat-lying sea-floor datum. These bathymetrically stripped response functions were then inverted without the need to incorporate bathymetry into the model. The bathymetrically corrected transfer tensor, although not identical to the original one, is also compatible with a 2D mantle having a strike coincident with that of the ridge. A finite difference 2D algorithm using a nonlinear minimization algorithm based on a steepest gradient method was used to invert these data (*26*, *27*). Several starting models were used, including a uniform half-space and the 1D model used to compute the electromagnetic distortion. The electric and magnetic fields were calculated independently to allow the TE and TM modes to be calculated from electric and magnetic fields at different sea-floor sites. The final results were not dependent on the choice of starting model. The preferred model (Fig. 3B) shows a reasonable fit everywhere at the 95% confidence level except for the TM mode phase at site M at periods shorter than 2000 s and at site Q between 3000 and 10,000 s. As for the RRI result, the misfit for a joint TM and TE model inversion can be improved when a single mode is considered alone. The first-order features of these single-mode inversions are similar to the joint inversion model. Some of the differences between the TE and TM mode models may have geological significance, such as those arising from anisotropy or along ridge heterogeneity in the mantle electrical structure.

The primary feature that is contained in both inversion models of Fig. 3 is a sharp asymmetry in mantle structure to the east and west of the ridge crest. Although they are not shown here, comparable asymmetry is also apparent in single-mode inversions of the TE and TM mode data. Further, the two models differ only in detail, but they will be described separately for completeness.

For the RRI model (Fig. 3A), the region immediately to the east of the ridge extending off-axis to about 150 km, and between depths of 20 and 120 km, is significantly more resistive than the adjacent mantle to the west. A conductive anomaly is found to the west of the ridge between 80 and 150-km depth with a width of about 50 km and centered around 50 km off-axis. Two conductive regions are found to the east of the ridge, one at about 180-km depth and about 50 km from the ridge axis and the other at the easternmost limit of the model (250 to 350 km) and at a depth of around 100 km. Limited data coverage further west than about 100 km from the ridge results in the RRI algorithm forcing the model to be 1D in this region.

In the model derived from topographically stripped data (Fig. 3B), the area west of the ridge also contains a resistive lithosphere and upper mantle extending to about 70 km depth, beneath which the structure becomes very conductive. To the east of the ridge, the uppermost mantle is more resistive, and these high resistivities extend deeper to around 100 to 120 km immediately east of the ridge but with shoaling to the east. A large conductive body is observed at depths greater than 100 to 120 km, beginning about 100 km to the east of the ridge. A number of sensitivity tests have been run on the resistivity structure over the depths important for melt generation, and by so doing have placed constraints on the structures included in the model. The conductive region at depth to the east of the ridge is required by the data. Increasing the resistivity of this feature causes an increase primarily in the TM mode misfit but also in the TE mode misfit at short periods. Most importantly, the minimum resistivity of the resistive block to the east of the ridge is constrained at least to a depth of 70 km, and it can be more resistive than is shown in the model.

Electrical resistivity in the crust and mantle varies over several orders of magnitude and is dependent on temperature which, to first order, is well known. To remove some of these effects from the models and place the resistivities within them in a broader geological context, they have been referenced against two profiles (Fig. 4). The first is based on laboratory measurements of the electrical resistivity of single crystals of olivine and on samples of peridotite under mantle temperatures and pressures (*28*). These resistivities, referred to as the SO2 data set, have been projected onto a sea-floor geotherm for 100-million-year-old lithosphere and have been used to compute a predicted resistivity depth profile. The second reference profile is based on the inversion of an MT response obtained with a basin-scale electric field measurement reported in (*29*) for the northeastern Pacific Basin, hereinafter referred to as LM. This profile represents an average resistivity structure for the Pacific Basin.

Differences between the ridge models and a dry-olivine resistivity profile could be due either to variations in thermal structure, to the influence of volatiles such as hydrogen, or to the presence of melt. Differences between the models and LM are probably the result of excess water (possibly at different depths), to the presence of melt, or to the effects of anisotropy if the difference is larger in the TM mode. Further, the greatest impact of temperature on resistivity will be associated with the formation of lithosphere and so is not of great importance from the perspective of melt generation and transport. The differences between the two inversion models and the LM profile are shown in Fig. 5.

In general, the mantle at depths between 60 and 120 km in a region about 40 km to the east of the ridge crest and extending to about 200 km east of the ridge is consistent with a dry olivine mantle. This is in contrast to the

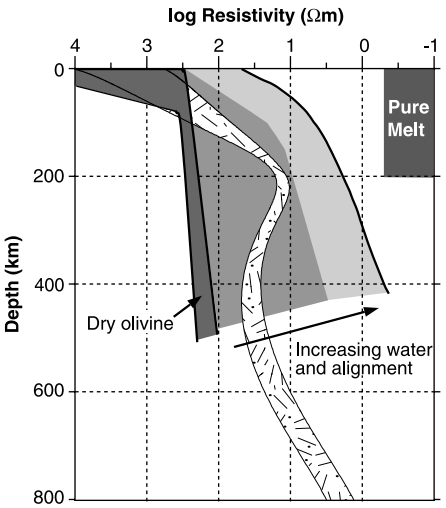

Fig 4. Reference resistivity profiles for the oceanic mantle. The dry olivine profile is based on the SO2 laboratory resistivity data (*28*) projected onto a sea-floor geotherm. The shaded profile (referred to as LM in the text) represents an average resistivity profile across the northeastern Pacific (*29*). One explanation for the peak in conductivity at 200-km depth is that it is caused by an anisotropic olivine fabric with 1000 H/10^6 Si in the form of dissolved hydrogen. This estimate is consistent with petrologic constraints on the amount of water in the mantle (*39*). The dark gray region represents the potential influence of dissolved hydrogen on an isotropic olivine mantle, whereas the light gray region shows the additional enhancement possible along the *a* axis of olivine in an anisotropic fabric. The region labeled as pure melt is included to demonstrate the marked enhancement of conductivity possible in the presence of melt (*40*), although how melt affects bulk conductivity depends on how it is distributed through the mantle and in particular on the connectivity of the melt network (*16*, *21*).

mantle elsewhere beneath this portion of the EPR and, for that matter, anywhere else that oceanic mantle resistivity has been measured (*29*). Given that any water present in the mantle is expected to be partitioned into the generated melt (*17*–*18*), an obvious explanation for this structure is that the mantle east of the ridge is dry and has had melt extracted from it. Another explanation is that there is melt within this part of the mantle but that it is sitting in isolated, unconnected pockets that do not affect the electrical conductivity. In fact, a small amount of melt distributed in this way would be one means of reconciling the MT and seismic results. In contrast, the region about 50 km to the west of the ridge, and centered around 100-km depth, is more conductive than either the SO2 profile or LM. This region might represent a zone of melting with a fully interconnected melt fraction of no more than about 3% melt within the center of the region and generally 1 to 2% melt surrounding it. This part of our model is consistent with the seismic results, although MT data coverage to the west is limited to within about 100 km of the ridge, and so it is not possible to identify whether the conductive anomaly extends as far to the west as the seismic low-velocity region.

The asymmetric resistivity structure may be directly related to the differences in spreading rate between the Pacific and Nazca plates. The resistive structure to the east of the ridge may be due to focused melt delivery beneath the ridge with the bulk of the mantle at depths between 40 and 100 km showing a melt-depleted and dehydrated structure that is circulating around its centroid (*5*, *6*). In contrast, the region to the west of the ridge may contain a small amount of melt distributed over a broad region of mantle, at least to 150 km west of the ridge, and with an additional and stronger anomaly around 100-km depth. Refinement of this interpretation is predicated upon modeling of mantle flows under asymmetric spreading conditions. These models will also need to incorporate the additional complications of mantle viscosity structure through dehydration, which in this case might cause lateral viscosity variations. Motion of the ridge axis to the west could also mean that the mantle beneath the Nazca plate has already melted, explaining its high resistivity.

In keeping with the seismic model, there is no evidence in the MT data for a narrow column of melt beneath the ridge crest; however, forward modeling suggests that a conductive column with a width of less than about 10 km containing 5 to 10% interconnected melt would not be discernible.

A conductive region at around 200 km depth offset to the east of the ridge is an intriguing feature of the resistivity model. It is more conductive than LM and is suggestive of deep incipient melting in the presence of water that has been offered as an explanation for incompatible trace element patterns in MORB (*3*). How this melt might be transported upward to the ridge crest is not clear from the resistivity model, as there is no discernible conductive feature that connects this region of the mantle to shallower points beneath the ridge crest. It is possible that melt might be transported in vertically oriented, tubelike regions whose vertically anisotropic conductivity would not impact the MT response. The MT method, which uses primarily horizontally flowing electric currents as its source, does not have much sensitivity to conductivity in the vertical direction. A series of vertical conductive pipes might be expected to have limited impact on both the TE and TM modes and thus not give rise to an observable change in the MT response tensor.

A possible interpretation of the conductive region 300 to 400 km to the east of the ridge is that it reflects strain-induced anisotropy due to alignment of olivine grains. Although olivine itself does not exhibit a large anisotropy, the diffusion of hydrogen is faster in the *a* crystallographic axis of olivine (*30*), and so this interpretation requires the mantle to be hydrous. Because of the pressure dependence of water solubility in olivine, a saturated isotropic mantle cannot hold enough water at 100-km depth to explain the observed decrease in resistivity with respect to LM (*31*). Instead, a degree of anisotropy would be required, with the most conductive direction consistent with flow-induced alignment of olivine. This interpretation would be consistent with a pattern of passive upwelling to the west of the ridge and buoyant flow to the east, with substantial flow-induced straining of olivine around 100-km depth and 300 km off-axis (*7*). However, other explanations are possible, including melting and the effects of regional heterogeneity.

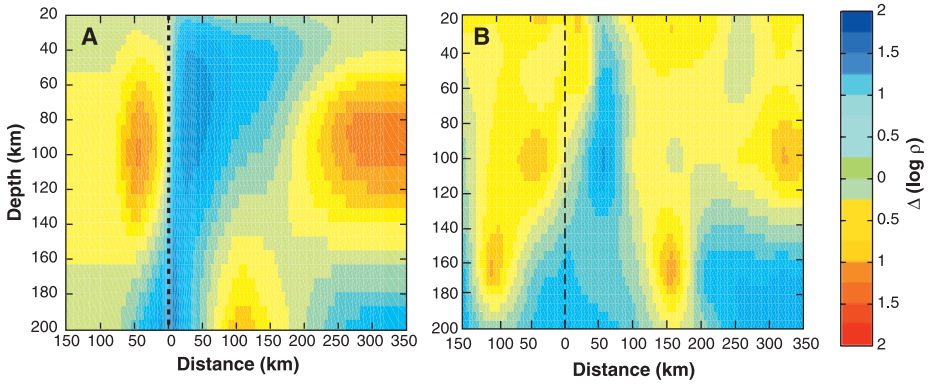

Fig. 5. Results of subtracting, in the logarithmic domain, LM from the models of Fig. 3 (**A** and **B**). The large region seen immediately to the east of the ridge is consistent with a dry-olivine structure. The conductive anomaly to the west of the ridge still appears, indicating that a modest amount of interconnected melt (1 to 2%) is required in this part of the mantle. Two other anomalies, one around 200-km depth just to the east of the ridge and another at 100-km depth some 300 km off-axis, are more conductive than LM. The deeper anomaly may indicate deep incipient melting in the presence of water. The anomaly to the east will require further analysis for it to be completely understood, although possible explanations are discussed in the text.

References and Notes

1. P. C. Hess, in *Mantle Flow and Melt Generation at Mid Ocean Ridges*, J. Phipps-Morgan, D. K. Blackman, J. Sinton, Eds. (American Geophysical Union, Washington, DC, 1992), p. 67.
2. V. J. M. Salters and S. R. Hart, *Nature* **342**, 420 (1989); P. D. Beattie, *ibid.* **363**, 63 (1993).
3. P. J. Wyllie, *J. Geophys. Res.* **76**, 1328 (1971); D. P. McKenzie, *J. Petrol.* **25**, 713 (1985); *Earth Planet. Sci. Lett.* **74**, 81 (1985); S. J. G. Galer and R. K. O'Nions, *Chem. Geol.* **56**, 45 (1986).
4. D. R. Scott and D. J. Stevenson, *J. Geophys. Res.* **94**, 2973 (1989); M. W. Spiegelman and D. P. McKenzie, *Earth Planet. Sci. Lett.* **83**, 137 (1987).
5. D. R. Scott, in (*1*), p 327.
6. W. R. Buck and W. Su, *Geophys. Res. Lett.* **16**, 641 (1989).
7. M. G. Braun, G. Hirth, E. M. Parmentier, *Eos* **78**, 693 (1997).
8. D. W. Forsyth and A. D. Chave, *ibid.* **75**, 537 (1994).
9. D. S. Scheirer *et al.*, *Science* **280**, 1221 (1998).
10. K. Perrot, thesis, Universite de Bretagne Occidentale, Brest, France (1998).
11. MELT Seismic Team, *Science* **280** 1215 (1998).
12. D. R. Toomey *et al.*, *ibid.*, p. 1224.
13. D. W. Forsyth *et al.*, *ibid.*, p. 1235.
14. S. C. Webb and D. W. Forsyth, *ibid.*, p. 1227.
15. J. P. Canales *et al.*, *ibid*, p. 1218; C. J. Wolfe and S. C. Solomon, *ibid.*, p. 1230; Y. Shen *et al.*, *ibid.*, p. 1232.
16. T. J. Shankland and H. S. Waff, *J. Geophys. Res.* **82**, 5409 (1977).
17. S. Karato, *Nature* **347**, 272 (1990).
18. J. G. Hirth and D. L. Kohlstedt, *Earth Planet Sci. Lett.*, **144**, 93 (1996).
19. J. H. Filloux, in *Geomagnetism*, J. Jacobs, Ed. (Academic Press, New York, 1987), vol. 1, pp. 143–248.
20. After initial data editing, a linear frequency-domain transfer tensor between the vector horizontal electric and horizontal magnetic field at each site oriented in a ridge strike coordinate system was computed with a bounded influence estimator (*32*) to eliminate outlier and leverage point contamination. The estimate was remote referenced to remove downward bias by local magnetometer noise using an adjacent sea-floor magnetic field record. Nonparametric standard errors on the elements of the transfer tensor were estimated with the jackknife (*33*). The magnitudes of the off-diagonal elements of the tensor are expressed as apparent resistivity, which reduces to the true resistivity of the medium for a half-space conductor.
21. R. L. Evans and M. E. Everett, in (*1*), p. 353.
22. These effects are often explained by frequency-independent galvanic distortion of the electric (*34*) and, especially for sea-floor data, magnetic (*35*, *36*) fields. When a galvanic model is appropriate, distortion may be removed using a tensor decomposition

(*35*). In some instances, this approach may fail because of a breakdown of the galvanic assumption, and a direct integral equation modeling approach to remove bathymetric distortion is required (*37*). A tensor decomposition (*35*) was fit to the data but found to have little effect at all periods. In fact, the uncorrected MT tensor displays most of the characteristics of a 2D medium with a strike direction coincident with that of the ridge.

23. J. T. Smith and J. R. Booker, *J. Geophys. Res.* **96**, 3905 (1991).
24. For the inversion algorithm to achieve satisfactory convergence, the target error level has to be larger than 1 SD, probably due to the influence of local topography that is not incorporated in the model, especially large-scale, fault-controlled valleys and seamounts. This is especially true for the apparent resistivity due to static shift, in which the observed amplitude is uncertain by a frequency-independent scale factor. For this reason, error levels on apparent resistivity were increased by a factor of 3 to emphasize fitting the phase. Other inversions were also carried out placing different relative weights on the observed apparent resistivities and phases and selectively downweighting stations that are close to large local topographic features to ensure that the first-order deep structures are retrieved regardless of error levels and achieved misfit value. In addition, the preferred model was derived by setting error thresholds of 5% on apparent resistivity and 5% on phase; this means that individual error estimates smaller than the prescribed threshold are increased to this value, but are left unaltered otherwise.
25. The electromagnetic distortion was computed numerically from the measured bathymetry (*9*) using a thin sheet of spatially variable conductance to simulate depth variations of the ocean. The area between longitudes 110°W and 115°W and latitudes 15°S and 18°S was discretized into 2-km by 2-km square cells and converted into a conductance map. The conductance in a given cell is simply the water depth times an average seawater conductivity of 3.3 S/m. The bathymetric distortion model also depends on the conductivity structure of the mantle, but previous work has shown that mutual coupling between surficial inhomogeneities and deep-mantle lateral heterogeneities is weak (*38*). Hence, the distortion is primarily a function of the sea-floor topography, and a 1D mantle model suffices for the stripping process. This model includes a 50-km-thick lithosphere of resistivity 1000 ohm-m overlying a more conductive mantle with a resistivity decreasing monotonically from 200 ohm-m beneath 50 km and terminating in a 1 ohm-m half-space below 600 km. The confidence intervals on the corrected MT tensor were calculated using the nonparametric jackknife (*33*).
26. J. H. Filloux, *Rev. Geophys.* **17**, 282 (1979); G. Fischer and B. V. LeQuang, *Geophys. J. R. Astron. Soc.* **67**, 257 (1981).
27. The χ^2 misfit measures the difference between the observed and calculated real and imaginary parts of the TE and TM impedances. The penalty function minimized is the sum of the χ^2 misfit plus the squared norm of the log conductivity gradient multiplied by a damping parameter adjusted so that the regularizing term is not overemphasized.
28. S. C. Constable, T. J. Shankland, A. Duba, *J. Geophys. Res.* **97**, 3397 (1991).
29. D. Lizarralde *et al.*, *ibid.* **100**, 17837 (1995).
30. S. J. Mackwell and D. L. Kohlstedt, *ibid.* **95**, 5079 (1990).
31. Q. Bai and D. L. Kohlstedt, *Nature* **357**, 672 (1992).
32. A. D. Chave and D. J. Thomson, *J. Geophys. Res.* **94**, 14215 (1989); _____, in preparation.
33. D. J. Thomson and A. D. Chave, in *Advances in Spectral Analysis and Array Processing*, S. Haykin, Ed. (Prentice-Hall, Englewood Cliffs, NJ, 1991), pp. 58–113.
34. R. W. Groom and R. C. Bailey, *J. Geophys. Res.* **94**, 1913 (1989).
35. A. D. Chave and J. T. Smith, *ibid.* **99**, 4669 (1994).
36. S. N. White, A. D. Chave, J. H. Filloux, *J. Geomagn. Geoelectr.* **49**, 1373 (1997).
37. G. Vasseur and P. Weidelt, *Geophys. J. R. Astron. Soc.* **51**, 669 (1977); R. Nolasco *et al.*, *J. Geophys. Res.* **103**, 30287 (1998).
38. M. Menvielle, J. C. Rossignol, P. Tarits, *Phys. Earth Planet. Int.* **28**, 118 (1982); P. Tarits and M. Menvielle, *Can. J. Earth Sci.* **20**, 537 (1983); A. Terra, thesis, Université de Paris VII (1993).
39. D. R. Bell and G. R. Rossman, *Science* **255**, 1391 (1992).
40. J. J. Roberts and J. A. Tyburczy, *J. Geophys. Res.* **104**, 7055 (1999).

41. We thank K. Baba, L. Banteaux, J. Bailey, A. Dubreule, T. Goto, R. Handy, H. Moeller, R. Petitt, B. Perkins, D. Shinn, and R. Walker for technical assistance. We also thank R. Detrick, G. Hirth, S. Webb, and two anonymous reviewers for helpful comments. U.S. instrumentation and participation in the MELT Experiment was funded by NSF grants OCE-9300117 and OCE-9402324, respectively. French participation was made possible by support from CNRS-INSU and by technical support from DT-INSU, Garchy. Australian support came from Australian Research Council grant A39331792 and a Queen Elizabeth II fellowship. Japanese scientists were supported by grant 07041089 from the ministry of Education, Culture and Science.

25 June 1999; accepted 8 September 1999

Subtropical North Atlantic Temperatures 60,000 to 30,000 Years Ago

Julian P. Sachs* and Scott J. Lehman

A reconstruction of sea surface temperature based on alkenone unsaturation ratios in sediments of the Bermuda Rise provides a detailed record of subtropical climate from 60,000 to 30,000 years ago. Northern Sargasso Sea temperatures changed repeatedly by 2° to 5°C, covarying with high-latitude temperatures that were previously inferred from Greenland ice cores. The largest temperature increases were comparable in magnitude to the full glacial-Holocene warming at the site. Abrupt cold reversals of 3° to 5°C, lasting less than 250 years, occurred during the onset of two such events (Greenland interstadials 8 and 12), suggesting that the largest, most rapid warmings were especially unstable.

Annually dated records of isotope paleotemperature from Greenland ice cores depict a highly volatile climate during the last glacial period [80,000 to 10,000 years ago (ka)] (*1*). Many of the largest temperature excursions occurred from 60 to 30 ka during marine isotope stage (MIS) 3, an interval characterized by intermediate ice sheet size, high-latitude radiation receipts, and atmospheric CO_2 concentrations. Similar excursions are seen in faunal records of high-latitude sea surface temperature (SST) (*2*) and geochemical records of deep ocean ventilation (*3, 4*), consistent with numerical modeling results showing a large dependence of high-latitude sea and air temperatures on the rate and mode of ocean thermohaline circulation (*5*). There are also indications of related SST change at lower latitudes (*6–8*), but these are primarily based on planktonic foraminiferal isotope records that may be influenced by factors other than temperature. The SST of the warm ocean is nonetheless expected to play a crucial role in amplifying and propagating climate change because the partial pressure of water vapor, an abundant and effective greenhouse gas, depends exponentially on temperature (*9*). Here, we present alkenone-derived SST records from Bermuda Rise sediments in the northwest Sargasso Sea and from high-deposition rate sites in the southwest Sargasso Sea in order to evaluate the temperature history of the subtropical Atlantic Ocean during MIS 3.

The Bermuda Rise is a sediment drift deposit northeast of the islands of Bermuda. Lateral sediment focusing within the North American Basin augments deposition at the site (*10*), so that late Quaternary sedimentation rates range from 10 to 200 cm/1000 years (1 ky) (*11*), some 5 to 100 times the open ocean average. As a result, Bermuda Rise sediments provide exceptional resolution in time. Core MD95-2036 (from 33°41.444′N, 57°34.548′W, at a water depth of 4462 m) is 52.7 m in length and contains sediments of Holocene through penultimate glacial (MIS 6) age (*11*). We determined SSTs by alkenone paleothermometry (*12*) in contiguous 1- or 2-cm intervals throughout the 12-m section of the core corresponding to MIS 3. Sedimentation rates averaged 30 cm/ky during the interval, so that single samples represent 33 to 67 years of deposition on average.

Lipids were extracted from 1 to 4 g of freeze-dried sediment with a pressurized fluid extractor, and alkenone abundances were quantified by gas chromatography with flame-ionization detection (*13*). Down-core results are presented in Fig. 1 in units of the alkenone unsaturation ratio ($U^{k'}_{37}$) and as estimated SSTs from the regression relation of Prahl and others (*12, 14*). Our semiautomated analytical procedure allows the routine analysis

Institute of Arctic and Alpine Research, University of Colorado, Boulder, CO 80309–0450, USA.

*Present address: Department of Environmental Science, Barnard College, Columbia University, 3009 Broadway, New York, NY 10027, USA.